A high-fidelity comprehensive framework for the additive manufacturing printability assessment

Liping Guo[1,2], *Hanjie Liu*[1,2], *Hongze Wang*[1,2,3,]*, *Qianglong Wei*[1,2], *Jiahui Zhang*[4], *Yingyan Chen*[1,2], *Chu Lun Alex Leung*[5,6], *Qing Lian*[1,2], *Yi Wu*[1,2,3,]*, *Yu Zou*[4], *Haowei Wang*[1,2,3]

1 State Key Laboratory of Metal Matrix Composites, Shanghai Jiao Tong University, Shanghai, 200240, China

2 School of Materials Science & Engineering, Shanghai Jiao Tong University, Shanghai, 200240, China

3 Institute of Alumics Materials, Shanghai Jiao Tong University (Anhui), Huaibei, 235000, China

4 Department of Materials Science and Engineering, University of Toronto, Toronto, ON M5S 3E4, Canada

5 Department of Mechanical Engineering, University College London, London, WC1E 7JE, UK

6 Research Complex at Harwell, Harwell Campus, Oxfordshire, OX11 0FA, UK

*Email: Hongze Wang, hz.wang@sjtu.edu.cn; Yi Wu, eagle51@sjtu.edu.cn

Abstract

Additive manufacturing is capable of fabricating complex and customized components that cannot be easily and economically produced by other techniques. It is of great significance to determine the printability map for the extensive application of the fabricated parts, which has been hindered by the common defects such as interior pores and surface roughness. Here, a comprehensive framework including multiphysics model, physics-informed machine learning, and experimental data is proposed to predict the printability. The characteristics for different phenomena (lack of fusion, balling and keyhole) are analyzed by the mechanistic model considering high-fidelity powder-scale model, fluid flow, recoil pressure and Marangoni effect, which provides a more accurate thermal history, molten pool dynamics and surface morphology compared to the finite element model. Classification criterion is established by three mechanistic variables based on the molten pool morphology, which divides the process map into four regions. For the first time, the relationship between the solidified-track surface morphology and the interior quality is established, and the optimal surface morphology corresponding to defect-free printing is determined. The printability is predicted by mathematical machine learning classification models via 10-fold cross-validation method, which validates the classification criterion and the comprehensive framework to assess the printability. This high-fidelity comprehensive framework to assess the printability could potentially guide the alloy design and printing parameters selection towards mass additive manufacturing production.

Keyword: printability, simulation, laser powder bed fusion, machine learning, surface topography

Nomenclature		P_r:	Recoil pressure
$\vec{v}$:	Velocity vector	$\vec{n}$:	Surface normal vector
ρ:	Density	h_c:	Heat transfer coefficient
t_s:	Time	σ:	Stefan-Boltzmann constant
p:	Pressure	ε:	Radiation emissivity
μ:	Kinematic viscosity	$\vec{v}_n$:	Normal velocity vector
F_d:	Drag force coefficient	γ:	Surface tension
$\vec{G}$:	Body acceleration	R_k:	Radius of curvature
h:	Enthalpy	μ_d:	Dynamic viscosity
k:	Thermal conductivity	l:	Length of molten pool
T:	Temperature	$w1$:	Width of molten pool from the top view
F:	Volume of the fluid	$w2$:	Width of molten pool on the upper surface of the substrate
q:	Laser heat flux	d:	Depth of the molten pool

1. Introduction

Laser powder bed fusion (LPBF) is a powder-based metal additive manufacturing (AM) technology fabricating parts layer by layer from a 3D computer-aided design model. Compared to subtractive manufacturing, it is capable of manufacturing parts with desired properties and high performance or to obtain specific surface structures [1-3]. The suitability of manufacturing by LPBF technology depends on two aspects, which can be described in terms of printability [4]. One is the intrinsic factors, including the secondary phase and solidification range that affect the microstructure. Tomus et al.

[5] studied the hot-cracking susceptibility of Hastelloy alloy and found that minor change of C and Si content reduced the hot-cracking tendency. Martin et al. [6] successfully printed high-strength aluminum which were not compatible with AM technology before by assembling nanoparticles onto alloy powders to control the solidification as nucleants.

The other is extrinsic processing factors that affect the overall consistency of the fabricated parts. The forming quality of the prepared parts is controlled by more than 130 processing parameters, of which the most frequently studied are laser power, scanning speed, etc [7]. The common defects in LPBF-produced parts are porosity and surface roughness, which are governed by the complex interaction between the high-velocity vapor, powder motion, and melt pool (MP) dynamics [8, 9]. These defects can adversely affect the structural integrity and mechanical properties, resulting in premature failure of parts [10, 11]. AM research has been primarily focused on finding useful combinations of these external factors, namely the printable region in the processing space [12]. As the solidified surface quality is dependent on the MP characteristics, it is reasonable to establish the thresholds for phenomena of lack of fusion (LOF), balling, and keyhole formation based on the MP morphology [4, 13]. Mukerjee et al. [14] established the printability indicators based on material characteristic, processing conditions and MP morphology. They identified several dimensionless parameters to estimate the susceptibility to the thermally induced distortion and the LOF interlayer pores. Scime and Beuth [15] developed a method to map MP defects to laser power and scanning speed, and to correlate the processing defects with the key features of the MP geometry. Johnson et al. [4] proposed printability metric for LPBF technique by finite element method, which was defined as the volume in the processing parameter space. However, the over-simplified conduction-only thermal model ignores the MP dynamics, and the randomly-packed powder bed was not included in the model. The fluid flow in MP determines the surface morphology of the solidification track, which in turn influences the surface finish of the final product. For example, it is well known that hump is caused by Plateau–Rayleigh instability [1, 16] and Kelvin-Helmholtz instability [8]. Moreover, the thermo-physical properties used in their model were not temperature-dependent. In addition to the above-mentioned problem of model accuracy, most of the current research on printability is solely focused either on interior quality based on MP morphology, or solidified track surface topography [4, 10, 15, 17], without establishing a relationship between interior quality and surface morphology. And there is currently no unified high-fidelity comprehensive framework to quantify printability intelligently.

I*n situ* imaging technologies (e.g., optical, infrared and X-ray imaging) have provided a unique ability to observe the MP evolution and fluid flow without disturbing the experiment process. Unfortunately, it is expensive and the MP information can only be obtained from the side. Numerical simulation appears to be the only viable and cost-effective way to address the challenge, which is increasingly used for MP dynamics investigation. Khairallah et al. [1] demonstrated the importance of recoil pressure and Marangoni convection in shaping the melt pool flow, and how denudation, spattering, and pore defects emerged by a high-fidelity simulation. Panwisawas et al. [18] established the additive manufacturability map based on the porosity, cooling rate and volatile mass loss via computational fluid dynamics modeling. Wang et al. [19] explained that the keyhole pore generation mechanism is the formation of transient bubbles and subsequent capture by the solidification interface by finite volume method. Papazoglou et al. [20] found that the energy density and plateau-Rayleigh capillary instability are the root causes for the balling formation of SS316 alloy. The mechanistic model for LPBF can provide physical information that leads to different solidified track qualities (LOF, good, balling and keyhole), such as MP morphology, temperature and velocity field. In the absence of understanding about the different phenomena formation mechanisms, but data on phenomena formation are available, machine learning (ML) [21, 22] can make valuable contributions in controlling parts quality. Training ML with physical data that captures physics behind different phenomena can provide important quantitative correlations between processing parameters and defects. Such correlations are important because they can largely reduce the number of experiments required to achieve high-quality parts.

In this paper, a comprehensive framework containing mechanistic modeling of additive manufacturing, physics-informed machine learning and experimental data is established to assess the printability. The 3D high-fidelity multi-physics model is built with the consideration of heat transfer, fluid flow, recoil pressure and Marangoni effect, and the formation processes of LOF, balling and keyhole are analyzed. Classification criterion is established by three mechanistic variables based on the molten pool morphology, which divides the process map into four regions. The relationship between the track surface morphology and the interior quality is first established and the optimal surface morphology corresponding to defect-free printing is determined. The printability is predicted by mathematical machine learning classification models via 10-fold cross-validation method.

2. Methodology

2.1 Physics-informed machine learning

During the fabrication of additive manufactured parts, LOF phenomenon occurs when the laser energy is insufficient to melt the substrate to a significant depth, which can result in large and sharp voids within the built part [23]. Balling or hump is a periodic oscillation of the solidified track caused by MP instabilities [24]. Such surface fluctuations are detrimental to powder spreading during subsequent layer processing, leading to the formation of interlayer voids [16]. Keyhole phenomenon is a depression formed on the surface of the MP due to the intense recoil pressure generated by the strong vaporization under the direct irradiation of the laser beam[9]. As these phenomena are related to the MP dynamics, it is reasonable to use several mechanistic variables based on MP morphology to represent the physics of various phenomena formation. In metal additive manufacturing, determining various phenomena by several mechanistic variables, which are based on physics and embody the influence of printing parameters, makes calculations tractable [25]. All these mechanistic variables can be calculated by a well-tested mechanistic model that considers fluid flow and powder evolution, providing further insight into the formation of several defects. Moreover, the combination of numerical simulation with data-driven machine learning through mechanistic variables can predict LOF, balling and keyhole phenomena, providing mechanistic insights that cannot be obtained by any other method (Fig. 1). It correlates different phenomena with mechanistic variables that can reveal the mechanisms underlying based on the laws of physics. Besides, the use of the physics-informed machine learning method will reduce the required amount of experimental data and cost, take full advantage of the powerful software and hardware capabilities of the digital age, leverages the rich knowledge base of metallurgy.

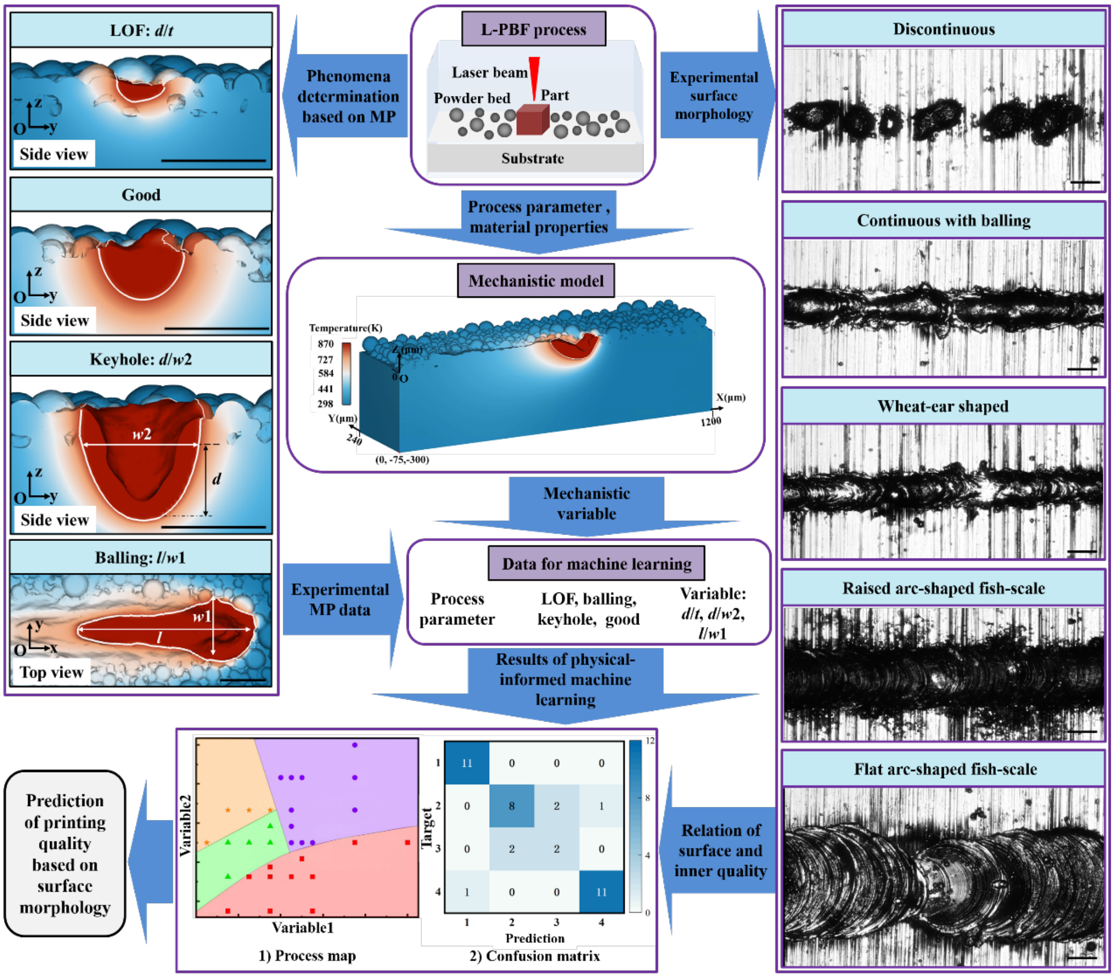

Fig. 1 Schematic of the comprehensive framework including multiphysics model, physics-informed machine learning, and experimental data to predict the printability. The surface morphology is divided into five types in the right column. The track quality is divided into four categories based on molten pool morphology in the left column, in which the symbols *l*, *w*1, *w*2 and *d* refer to the MP length, MP width on the top view, MP width on the upper surface of the substrate and MP depth, respectively. ‘Prediction’ represents the predicted output of the machine learning. ‘0’, ‘1’, ‘2’, and ‘3’ represent balling, good, keyhole and LOF, respectively. The scale bar is 100 μm.

2.2 Model

A high-fidelity computational fluid dynamics (CFD) model is established to visualize the printing process in LPBF using the commercial software Flow 3d. Details about the modeling and parameters used in the simulation, as well as the model validation can be found in the supplementary information. The powder bed is generated via the commercial software Particle Flow Code (PFC) based on the distinct element method (DEM). The particle size is in the range of 15-53 μm with D_{50}=33.09 μm, and the layer thickness is 30 µm. The computational domain is shown in Fig. 2 and it is meshed into cubic grid with size of 4*4*4 μm^3. Void refers to the region other than the fluid and has uniform ambient temperature and pressure. Red point in Fig. 2(a) shows the initial position of laser, moving along the x-direction.

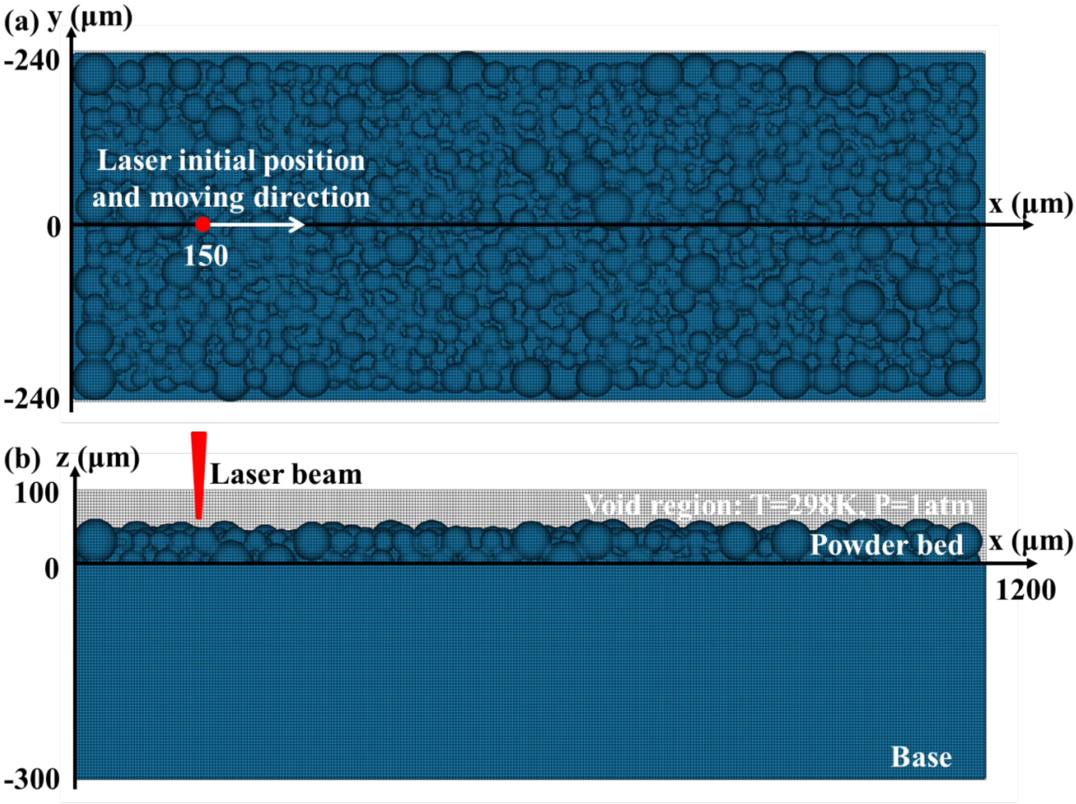

Fig. 2 Different views of the meshed computational domain and the coordinate system used in the simulation, (a) top view and (b) main view.

2.3 Mechanistic variable

Three mechanistic variables related to different phenomena (LOF, balling, and keyhole) are determined based on MP geometry, which are depth/layer thickness (d/t), depth/width ($d/w2$) and MP aspect ratio (MP length/MP width, $l/w1$), respectively. The values of these variables are calculated using the well-tested mechanistic model. Depth is defined to be the MP depth below the substrate. Regarding the keyhole formation criterion, the width refers to the MP depth on the upper surface of the substrate. Balling or hump determination criterion also reflected the fluctuation of MP. Therefore, the MP width and length are the data form the top view. A schematic representation of these symbols can be found in the upper left corner of Fig. 1.

Depth/layer thickness (d/t): A threshold of $d/t < 0.5$ is used to judge the LOF phenomenon, which was also used by Letenneur [26] and Johnson [4]. If the MP cannot penetrate deeply into the substrate to form a good bonding, discontinuous track or irregular and sharp LOF pores will be generated. On the other hand, the thicker the powder layer, the deeper the MP is required to penetrate into the substrate to form good bonding.

Depth/width ($d/w2$): The keyhole is a deep, narrow and key-like shape formed on the MP surface due to the large recoil pressure pushing the molten metal apart. There is an assumption of semicircular MP on the cross-section perpendicular to the laser moving direction when processing the isotropic materials under conduction mode [4]. Therefore, it can be deduced the keyhole criterion of depth/width > 0.5 is reasonable. Johnson et al. proposed depth/width > 2/3 as a better prediction due to the large heat loss in practice. As the depth used in this work is defined as the MP depth below the substrate, we can get $d/w2 > (2/3 - t/w2)$ by changing the above criterion. The keyhole threshold is defined as $d/w2 > 0.45$ in this work.

MP aspect ratio ($l/w1$): Balling or hump is formed due to the MP instability. When the length of the MP is significantly large than the width, it will become unstable and decompose into small balls or form humps [23]. This phenomenon can be determined by the MP aspect ratio and most of them are in the range between $2 < l/w1 < \pi$. The threshold for balling formation used in this study is defined as $l/w1 > 2.1$.

2.4 Data for Machine learning

In this work, the machine learning analysis is based on a dataset containing 31 data points of simulation results and 7 data points of experimental results collected under different power-scanning speed (P-V) combinations. Each data point is composed of three calculated variables along with the corresponding phenomenon (LOF, balling, good and keyhole). As the LPBF process is dynamically changed, the data used for machine learning analysis is the average values under different moments. Any P-V combination that is not labeled with these specific phenomena is marked as good type. The inputs of the machine learning model are different processing parameters. The laser power is in the range of 90-600 W and the scanning speed is in the range of 600-4000 $mm \cdot s^{-1}$. The dataset is supplied in the supplementary information in table s3. Classification is based on the process variables, and the output is one of the four phenomena. Decision tree (DT) and support vector machine (SVM) are employed to fulfill the classification task, due to their advantages of interpretable, statistically significant, and friendly to small datasets [27, 28]. 70% of the dataset are used for training and the left are used for validating. The 10-fold cross-validation is applied to eliminate the bias induced by splitting the dataset.

2.5 Experiment

The material used in this study is TB-AlSi10Mg (6wt% TiB_2-AlSi10Mg). The powder is fabricated by gas atomization with a diameter range of 15-53 μm. The single-track experiments are conducted on the machine Prox DMP 200 (3D system, USA) with a maximum laser output power of 300 W, a wavelength of 1070 nm and a focused laser beam diameter of 75 μm. A layer of powder is spread on the bare plate with a powder bed thickness of 30 μm. The laser moves along a straight line with a distance of 3 mm. The detailed fabrication process can be referred in Ref. [29, 30]. The experimental MP data points used for classification are obtained by microscopic telescope based on the single-track experiment. The detailed experimental data can also be referred in table s3.

3. Results and discussion

3.1 Formation process of different phenomena

In this section, the formation processes of LOF, keyhole and balling are analyzed via the mechanistic model, to reveal the fluid flow and MP characteristics.

3.1.1 LOF defect

Fig. 3 displays the MP evolution perpendicular to the laser moving direction. For the cases with a power of 90 W (a, b), only the upper surface melts, and the MP does not penetrate into the substrate, leaving a large amount of LOF voids indicated by the blue arrows. When the power increases to 195 W (c), the MP basically reaches the substrate, but the depth below the substrate is very small. As the power further increases to 225 W (d), it is still a weak bonding to substrate due to the small MP depth. Judged by the defect criteria, these four cases are all LOF conditions. It is apparent from the above analysis that the MP depth below the substrate (*d*) is an important indicator. For the situations that MP doesn't penetrate the substrate, *d* is zero, obviously that there is no effective bonding between the powder layer and the substrate. Even if the MP can just reach the substrate, considering the thickness of the solidified powder layer and the bonding to adjacent tracks in component fabrication, a small *d* is insufficient for high workpiece performance as LOF pores can be the sites for crack initiation and propagation, as well as stress concentrations [31]. The last column indicates that the height of the solidified track above the substrate decreases as the energy density increases, which can be attributed to that the molten metal flows downward to fill the

LOF voids.

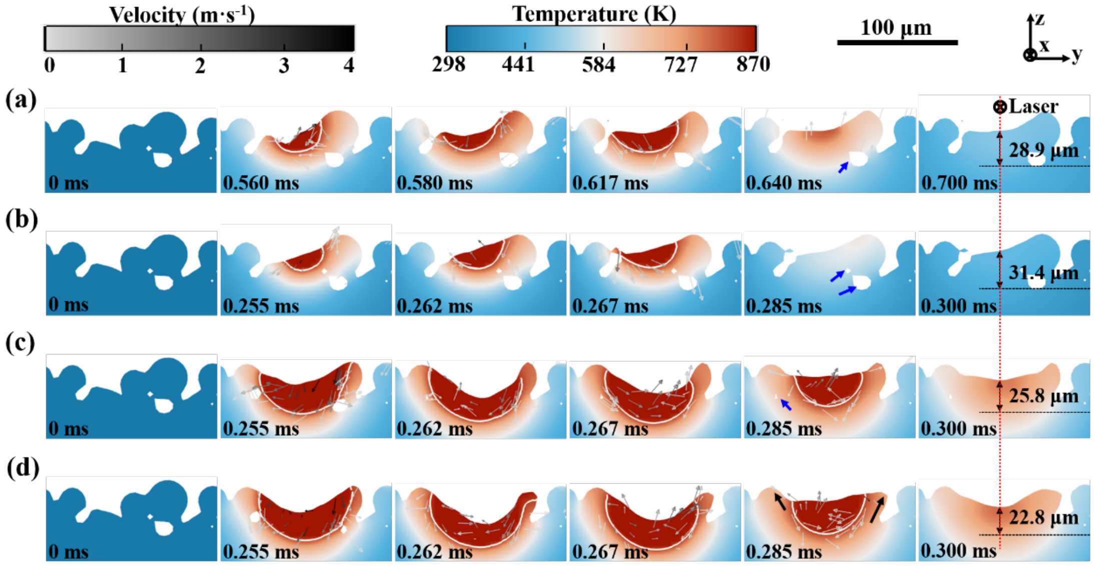

Fig. 3 MP evolution and fluid flow in the cross-section perpendicular to the laser moving direction for different power-scanning speed combinations of LOF cases, (a) 90 W-600 mm·s^{-1}, (b) 90 W-1400 mm·s^{-1}, (c) 195W-1400 mm·s^{-1}, (d) 225 W-1400 mm·s^{-1}. The blue arrows show the LOF pores and the black arrows indicate the unmelted region. The white lines are the MP boundary and the black dotted lines are the top surface of substrate. The height data in the last column indicates the solidified track height. The scale bar is 100 μm. (Supplementary videos 1- 3).

Fig. 4 shows the MP evolution parallel to the laser moving direction. For the case of 90 W (a, b), there exist a large number of LOF voids because the MP doesn't penetrate into the substrate. No obvious flow is observed due to the extremely small MP. When the power increases to 195 W (c) and 225 W (d), the powder melting degree (melting flow flux) also increases, and the recoil pressure pushes the fluid away to form a depression on the MP surface. There is a counterclockwise flow in the MP (marked in dotted yellow arrows), resulting in the fluid accumulation in the rear part. When the fluid accumulates to a certain height, the hydrostatic pressure increases, and the flow along the boundary to the right corner is strengthened. Then depression is filled and the liquid level becomes flat. It can be seen that there is only a counterclockwise flow in the MP, which may be due to the relatively small MP formed by insufficient energy density. A small MP is insufficient to wet the substrate well and to form a good bonding with the adjacent tracks.

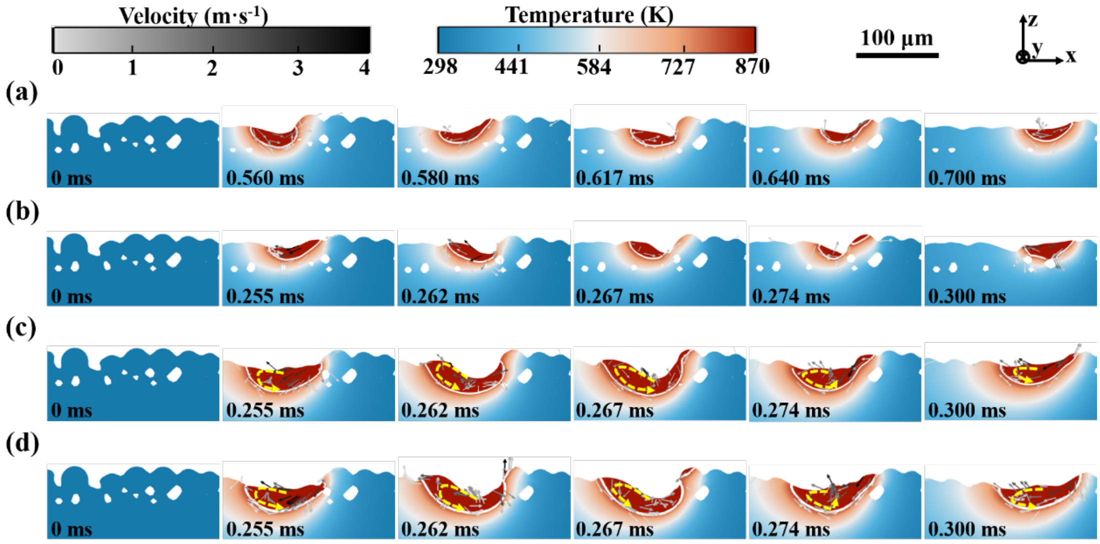

Fig. 4 MP evolution and fluid flow in the cross-section parallel to the laser moving direction for different power-scanning speed combinations of LOF cases, (a) 90 W-600 mm·s^{-1}, (b) 90 W-1400 mm·s^{-1}, (c) 195W-1400 mm·s^{-1}, (d) 225 W-1400 mm·s^{-1}. The dotted yellow arrows indicate the major flow. The white line is the MP boundary. The scale bar is 100 μm.

3.1.2 Keyhole phenomenon

Based on the phenomenon identification criterion, two cases belonging to keyhole condition are presented in Fig. 5 to reveal the MP evolution. Melting occurs as the laser irradiates to the powder. When the temperature goes above the boiling point, recoil pressure induced by the strong evaporation pushes the molten metal away to form the keyhole. The MP presents a longitudinally elongated arc shape due to mainly downward push of the recoil pressure, which is different from that (shallow MP) in the LOF situation discussed in 3.1.1 section. With the reducing of scanning speed, the depth and width of MP both increases, and the ratio of depth and width also increases (0.535 to 0.545, see table s3 in the supplementary information), resulting in the narrower and deeper keyhole. This implies that the main feature of the keyhole is the longitudinal elongation, and with the increase of the energy density, the longitudinal direction exhibits a larger increase rate than the transverse direction (described by $d/w2$). Therefore, $d/w2$ can be the characteristic index of keyhole. As the laser moves forward, the top surface is no longer exposed to the laser, resulting in a rapid decline of the temperature and recoil pressure. Due to the large curvature of the liquid surface, especially in the case of deep keyhole, the molten metal at the MP bottom is pulled upward under the action of surface tension, resulting in the liquid level to rise gradually.

After the liquid surface is relatively flat, the upward flow basically disappears due to the small curvature and surface tension.

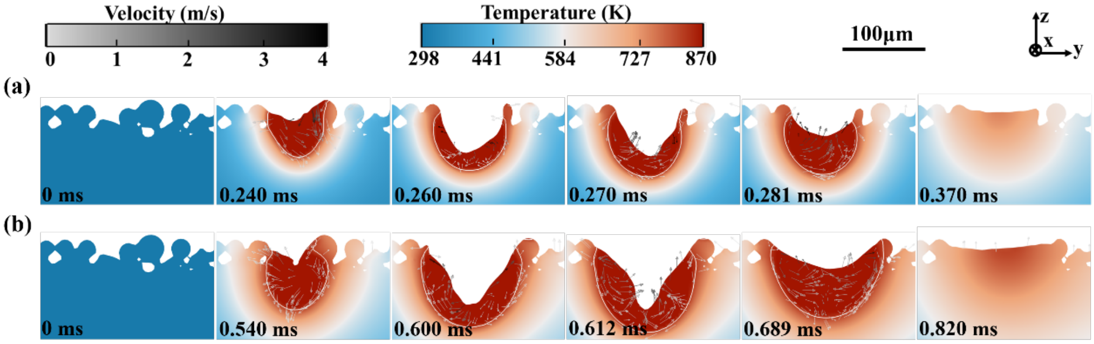

Fig. 5 MP evolution and fluid flow in the cross-section perpendicular to the laser moving direction for different power-scanning speed combinations of keyhole cases, (a) 400 W-1400 mm·s^{-1}, (b) 400 W-600 mm·s^{-1}. The white lines are the MP boundary. The scale bar is 100 μm. (Supplementary videos 4, 5).

The fluid flow and MP characteristic parallel to the laser moving direction are shown in Fig. 6. It is clearly that the flow can be divided into two stages. The first stage is the penetration of the keyhole, indicated by the depth of keyhole changing from minimum to maximum. When the depth is the smallest, the recoil pressure (Fig. 7) is huge and pushes the fluid to flow upward along the rear wall of the keyhole, only a counterclockwise flow formed in the MP behind keyhole. During the depth increasing stage, more and more fluid is pushed to and accumulates at the rear of the MP. When the keyhole depth is maximized, the recoil pressure driving the fluid backward is the minimum. The hydrostatic pressure at the tail of the MP reaches the maximum. The curvature is the largest and hence reducing the surface energy. At the second stage, the fluid flow mainly includes the forward flow along the bottom of the MP and the forward flow upwards towards the top of the MP, causing keyhole to be filled and the liquid level to rise. After the keyhole depth reaches the minimum again, the recoil pressure is the maximum and the flow mentioned above repeats. Under the same laser power, MP width and depth increase with the decrease of scanning speed (Fig. 5), and there will be more space in the MP for the fluid to flow. The solidified track is smoother (solidified track height fluctuation) in keyhole condition with the energy density increasing [8]. However, the solidified track height decreases compared with the height of the powder layer before melting, indicating that the fluid spreads too much under high energy density, which is not conducive to high-efficiency printing and well-formed track morphology.

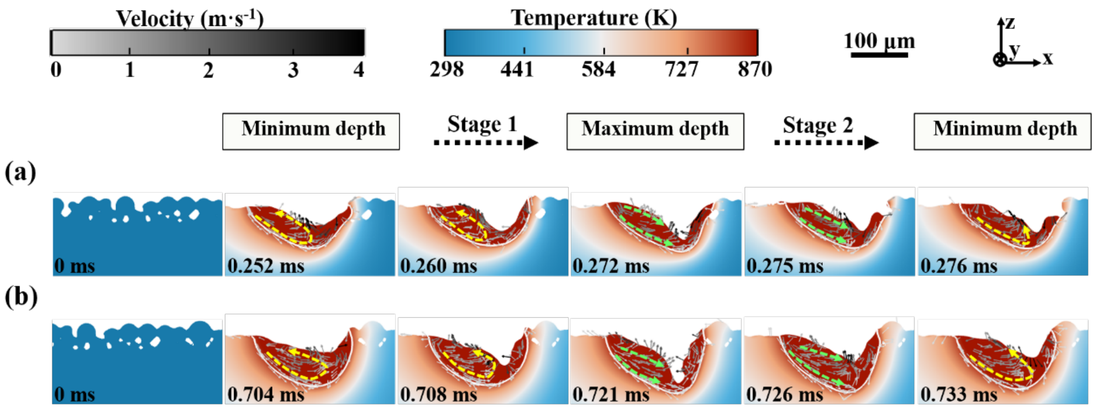

Fig. 6 MP evolution and fluid flow in the cross-section parallel to the laser moving direction for different power- scanning speed combinations of keyhole cases, (a) 400 W-1400 mm·s^{-1}, (b) 400 W-600 mm·s^{-1}. The white lines are the MP boundary. The yellow arrows indicate the counterclockwise flow in the keyhole depth increasing stage, and the green arrows indicate two flows in the keyhole depth decreasing stage. The scale bar is 100 μm.

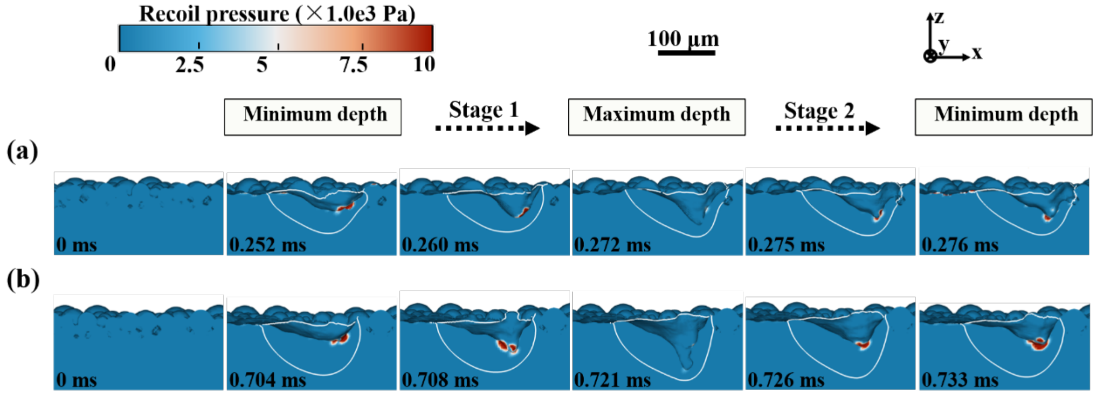

Fig. 7 Distribution of recoil pressure for different power- scanning speed combinations of keyhole cases, (a) 400 W-1400 mm·s^{-1}, (b) 400 W-600 mm·s^{-1}. The scale bar is 100 μm.

3.1.3 Balling effect

Balling, or hump, is a surface undulation or discontinuity of the solidified track. The MP evolution and fluid flow for the formation of this phenomenon are displayed in Fig. 8, which can be roughly divided into two stages. **i. Expansion**. The MP length at 0.181 ms is short. Under high power and high scanning speed, it suffers rapidly expansion especially in the length, resulting in an elongated spoon shape of the MP (from the top view). A deeper depression is formed and a large amount of fluid is pushed out of it due to the strong recoil force, gathering towards the rear of the molten pool. **ii. Pinched off**. With the increase of the hydrostatic pressure at the tail of the MP, combined with the viscous shear force, the resistance to the backward flow also increases. In order to reduce the surface tension, the thin liquid bead is preferentially broken up into separated droplets with small surface area. The pinch-off near the tail of the MP produces a solidified hump (0.261 ms) that manifests as Plateau-Rayleigh instability, and eventually forms balling phenomenon [24]. The MP length decreases sharply. The *in situ* experimental results by Umberto Scipioni also revealed that under high scanning speed and high-power conditions, other parts of MP (such as the central part) solidified relatively quickly, and the thin part in the center of the molten pool solidified ahead of the thick part, causing the broken up of the molten pool. The MP shape for balling phenomenon is elongated along the laser movement, which is obviously different from the shallow MP for LOF condition and the longitudinal elongated MP of keyhole. Therefore, the MP aspect ratio can be a characteristic indicator to distinguish the balling from other phenomena.

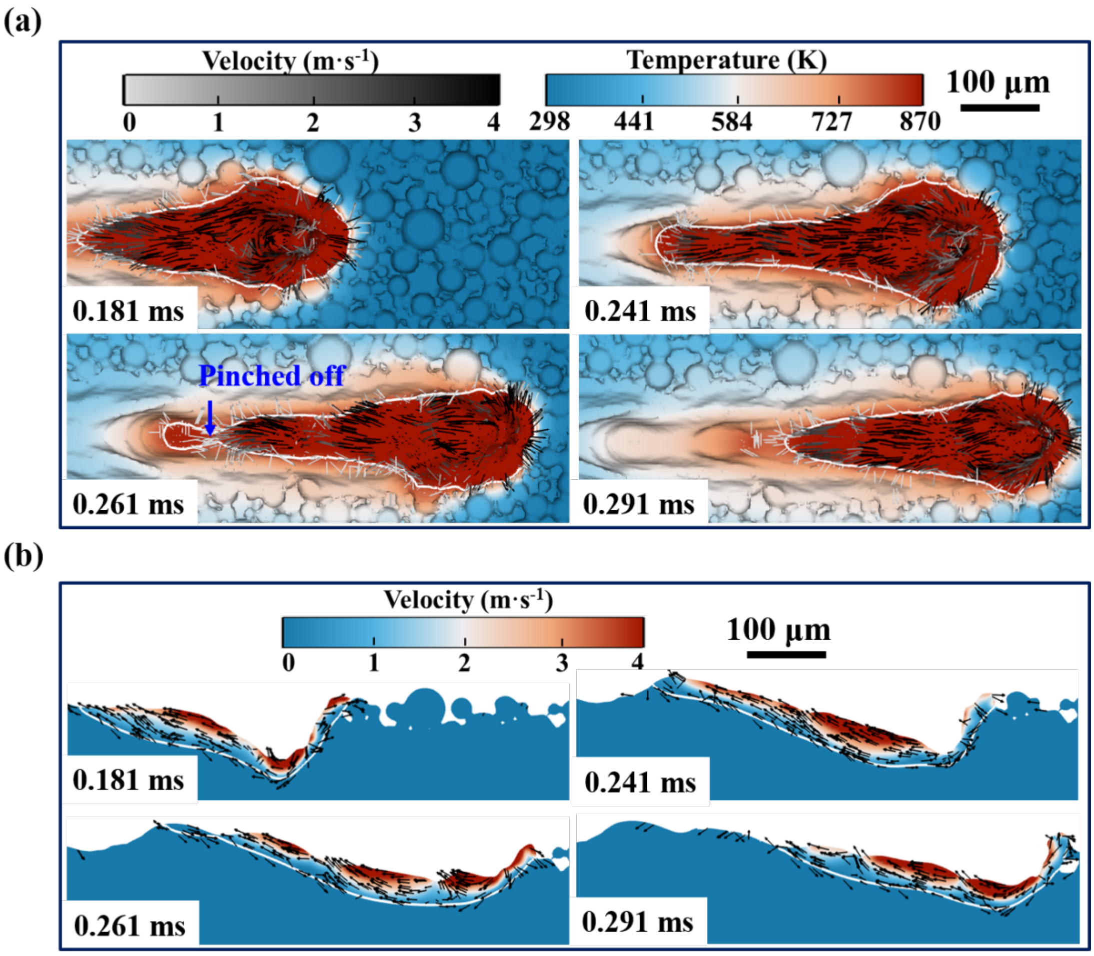

Fig. 8 (a) MP evolution and fluid flow from the top view and (b) Fluid velocity in the 2D clips parallel to the laser moving direction for balling phenomenon with P=600 W

and V=3000 mm·s^{-1}. The scale bar is 100 µm.

Fig. 9 demonstrates the MP evolution perpendicular to the laser moving direction for different P-V combination, which are classified as balling phenomenon based on the MP aspect ratio. For the case of 300W-4000 mm·s^{-1} (a), the depth of the MP below the substrate is around 8.5 µm, thus it can be identified as the LOF type as well. The MP shape is arc-shaped. For the case of 500W-3000 mm·s^{-1}, the MP depth below the substrate is about 35 µm, indicating a complete melting. A triangular-shaped MP can be observed in the initial stage of the MP formation. While for the case of 600W-300 mm·s^{-1}, the MP depth below the substrate is about 50 µm， and the depth/width ratio is 0.317, which is greater than the threshold value of 0.22. Therefore, it can be classified as balling as well as keyhole. The MP shows an obvious triangular shape at the beginning of its formation, which is significantly different from the MP shape in the keyhole state. The large recoil pressure pushes the free surface downward and large amounts of fluid accumulates at the rear part of the MP. After the laser leaves this cross-section, the liquid level rise gradually due to the surface tension. Before this cross-section solidifies, its position gradually changes from the front of MP to the middle of MP, and finally the rear of the MP. According to the top view in Fig. 9, large amount of fluid accumulates at the rear of the MP and eventually solidifies to form balling. The recoil pressure promotes the backward flow while the surface tension prevents the fluid from flowing backward, thus the competition between them determines the balling degree. The greater the energy, the more serious the fluid accumulation, leading to higher track height.

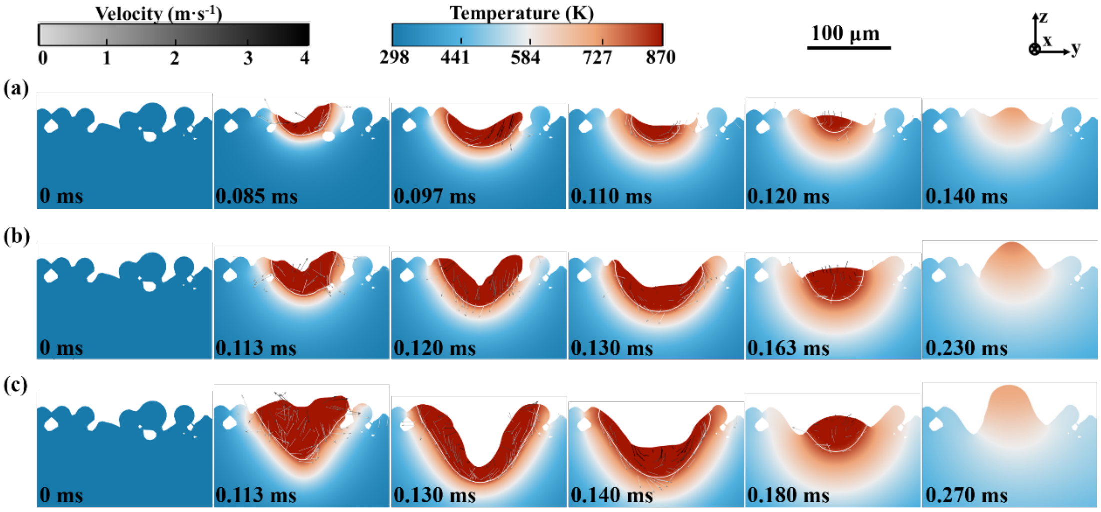

Fig. 9 MP evolution and fluid flow in the cross-section perpendicular to the laser moving direction for different power- scanning speed combinations of balling cases, (a)

300 W-4000 mm·s^{-1}, (b) 500 W-3000 mm·s^{-1} and (c) 600 W-3000 mm·s^{-1}. The white lines are the MP boundary. The scale bar is 100 μm.

Balling is the surface undulation phenomenon of the solidified track, and the standard deviation can determine the data dispersion. Therefore, the standard deviation of the track height can be used to identify the balling degree, as shown in Fig. 10. It is apparent that at a constant laser power, the balling degree increases with the increase of the scanning speed (3# (2200 mm·s^{-1})→2# (3000 mm·s^{-1})→1# (4000 mm·s^{-1})). This is because higher scanning speed leads to longer laser the path in a certain period time, resulting in larger MP aspect ratio (seen Fig. 10 (b)) and more unstable MP. Under the influence of Plateau-Rayleigh capillary instability, MP decomposes into small chain beads and gradually solidifies [24], leading to the larger track-height standard deviation. When the scanning speed is fixed, the balling degree increases with the increase of laser power (4# (400 W)→5# (500 W)→6# (600 W)). It can be attributed to that the case with larger power possesses greater MP aspect ratio and eventually the more unstable molten pool. Fig. 10 (c) shows the surface height relative to the upper surface of the substrate, and the insets are the profiles of the solidified track height along the center of the laser path. These figures provide further proof for the above analysis results.

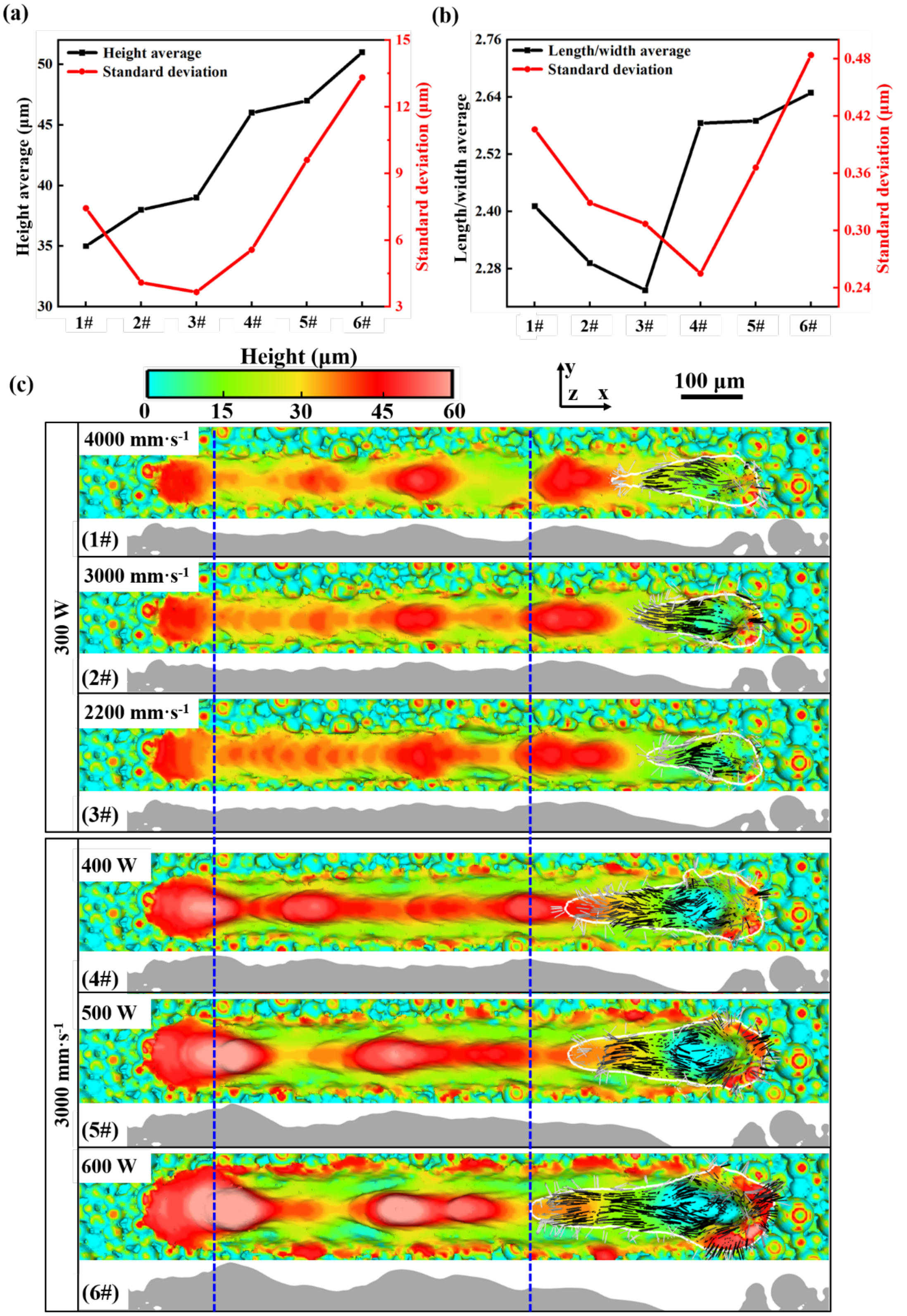

Fig. 10 Mechanistic variables of different P-V combinations belonging to balling defect, (a) average solidified track height and corresponding standard deviation, (b) average MP length/width ration and corresponding standard deviation, (c) surface height relative to the upper surface of the substrate. The insets in (c) show the profiles of the

solidified track height along the center of the laser path, in which the lower boundary of the box corresponds to the upper surface of the substrate. The track height is extracted every 20 μm along the laser path between the two dashed blue lines in (c). The scale bar is 100 μm. (Supplementary videos 6-11).

3.2 Printability map

The above analysis indicates that there exist some printing recipes classified as two phenomena simultaneously. In order to establish the process map (P-V) based on the MP mechanistic variables clearly, a further classification was made considered the actual track quality, shown in Fig. 11.

The first is the determination of LOF defect, a state of insufficient heat input, which is a P-V combination that should be avoided. In the LOF region, when the heat input is low, a phenomenon considered as balling defect due to the lack of melting of substrate and resulting spheroidization will occur. For example, the previously discussed 300W-3000 mm·s^{-1} and 300W-4000 mm·s^{-1} recipes belong to both LOF and balling according to the judgement criterion. This kind of balling, in which the MP does not penetrate deeply into the substrate, results in weak bonding. Therefore, it is divided into LOF defect. After the determination of full melting, the classification is based on whether it is balling. The undulation of the solidified track surface causes subsequent layers to have different remelting depth along the length of the track, resulting in different kinds of pores in the multilayer structure. The thickness of the solidified melting track fluctuates, and this inconsistent remelting reduces the uniformity of the multilayer component. For P-V combination at high power and high scanning speed, it might belong to both balling and keyhole simultaneously (previously discussed 600W-3000 mm·s^{-1}), but based on the uneven track, it is classified into balling. Then it comes to keyhole division, which is generated due to the excess heat input. The keyhole is divided into stable keyhole and unstable keyhole. Theoretically, only the unstable keyhole collapsing will lead to porosity. For the sake of energy efficiency and printing quality, both of these two regimes are referred as keyhole phenomenon in this work. Finally, after eliminating the above three phenomena, the rest can be classified as good.

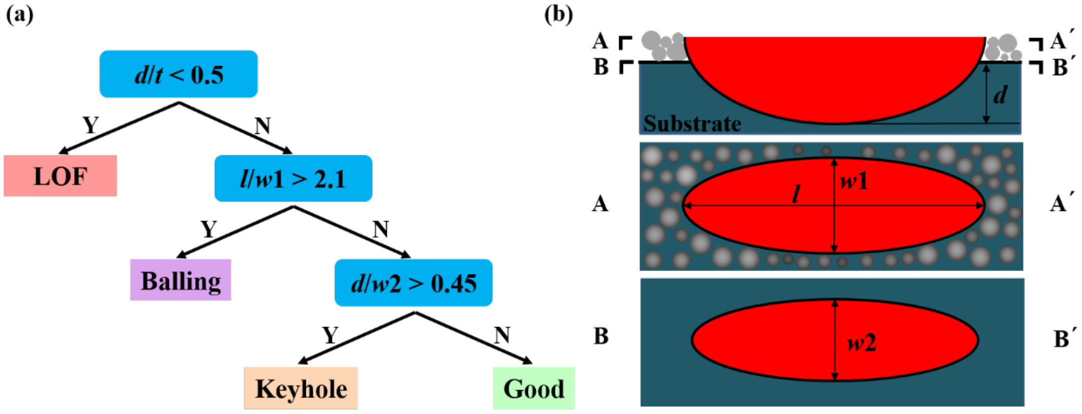

Fig. 11 (a) Classification procedure of four kinds of phenomenon based on the MP mechanistic variables and (b) schematic of the variables. For the sake of energy efficiency and printing quality, both stable and unstable keyhole are referred as keyhole phenomenon in this work.

3.2.1 Printability based on the mechanistic variables

For a given printing recipe, the mechanistic variables can be calculated by the multiphysics model, and the corresponding type can be determined by the above classification criteria. The 31 sets of simulated data and 7 sets of experimental data are divided into four categories, and then P-V map is obtained by origin, shown in Fig. 12. It can be seen from the figure that LOF defect (labeled as red region) tends to form in the lower right region, corresponding to the low heat input. Keyhole phenomenon (orange region) is prone to form at high power and low scanning speed, which can be attributed to excess heat input leading to intensive evaporation and strong recoil pressure. Balling effect (purple region) generates at high power and high scanning speed due to Rayleigh instability of the MP the with large aspect ratio. The printable region (green region) is the result of subtracting these three defect areas in P-V space. It can be seen from the process map that the classification based on the experimental data and the simulated data has good consistency (overlapping points of the black and other colors). The MP morphology of single-track experiment is displayed in Fig. 13.

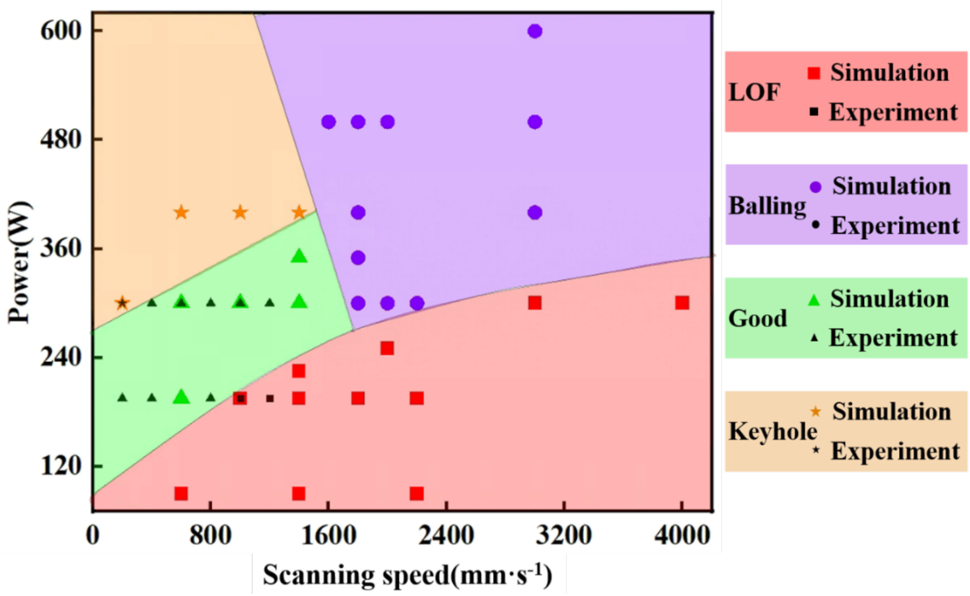

Fig. 12 Printability map identified by the mechanistic variables based on the MP. The black symbols are the experimental data points. The red, purple, green and orange symbols are the simulated results corresponding to LOF, balling, good and keyhole, respectively.

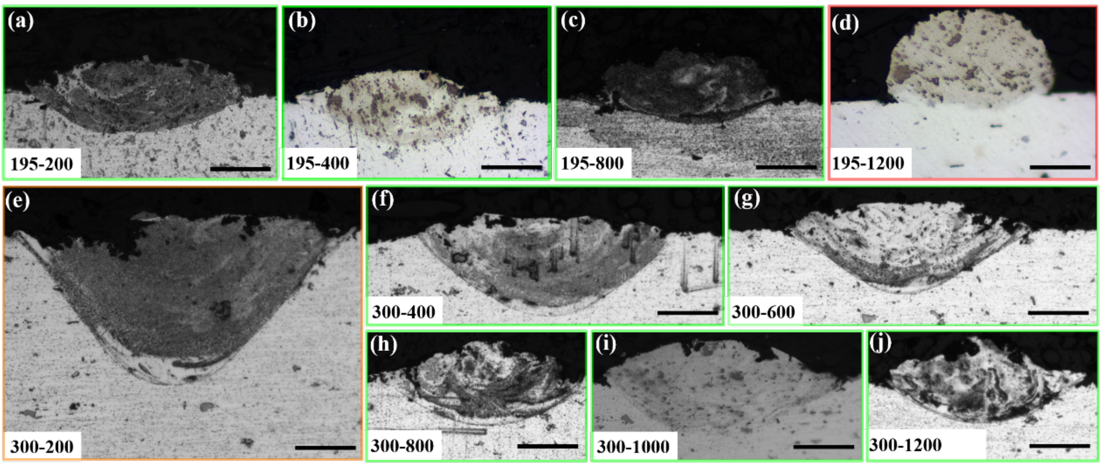

Fig. 13 Molten pool morphology of single-track experiments. The symbols on the lower left corner indicate the P-V combination (for example, 195-200 means 195W-200 mm·s^{-1}). The sub-pictures with green border (a-c, f-j), red border (d) and orange border (e) are classified as good, LOF and keyhole, respectively. The scale bar is 50 μm.

3.2.2 Printability based on the surface topography

In actual printing, the first observation is the surface morphology of the deposited track rather than the MP morphology. By classifying the surface topography and connecting with the printing quality (printability map based on the MP morphology), the quality of the formed track can be evaluated more easily without cutting and polishing the sample, which is of great significance for process optimization. The topological morphology of a single track is divided into five types, which are discontinuous, continuous with balling, wheat-ear shaped, raised arc-shaped fish-scale, and flat arc-shaped fish-scale, respectively [17]. It can be seen from Fig. 14 that the fourth type (raised arc-shaped fish-scale) falls in the printable region (green), indicating that this kind of surface morphology is the best choice in printing. When the power is 195 W, as the scanning speed increases, the surface morphology gradually changes to the third type (wheat-ear shaped), which falls in the LOF region (red). It indicates that this kind of topography belongs to incomplete fusion despite of a continuous track. When the speed is further increased, balling appears and still locates in the LOF region. It shows that the balling phenomenon under this processing parameter belongs to incomplete fusion, in other words, only the surface of the powder layer is melted, and then solidified into a ball under the effect of surface tension. Under the condition of 300 W and low velocity, it possesses a flat arc-shaped fish-scale pattern (fifth type), which falls in the keyhole region (orange), demonstrating an excessive heat input. It also confirms the analysis in the keyhole section that in the keyhole state, the track height decreases with the decrease of the scanning speed, and the track is smoother. With the further increase of the scanning speed, the surface morphology gradually changes from the fourth type to the second type, skipping the wheat-ear shaped topography, revealing that the balling under this processing parameter is mainly due to the Rayleigh instability.

The three red stars (S1, S2, S3) correspond to the surface morphology predicted by the relationship established above. The prediction results show that the surface morphology for S1, S2 and S3 should be the fourth type, third type and third type, respectively. The actual surface topographies for the three data points are in Fig. 14 (c), which are consistent with the predicted results, validating the classification of the surface topography and the connection between surface morphology and printing quality. It provides a good solution to judge the printing quality from the surface instead of from the cross-section.

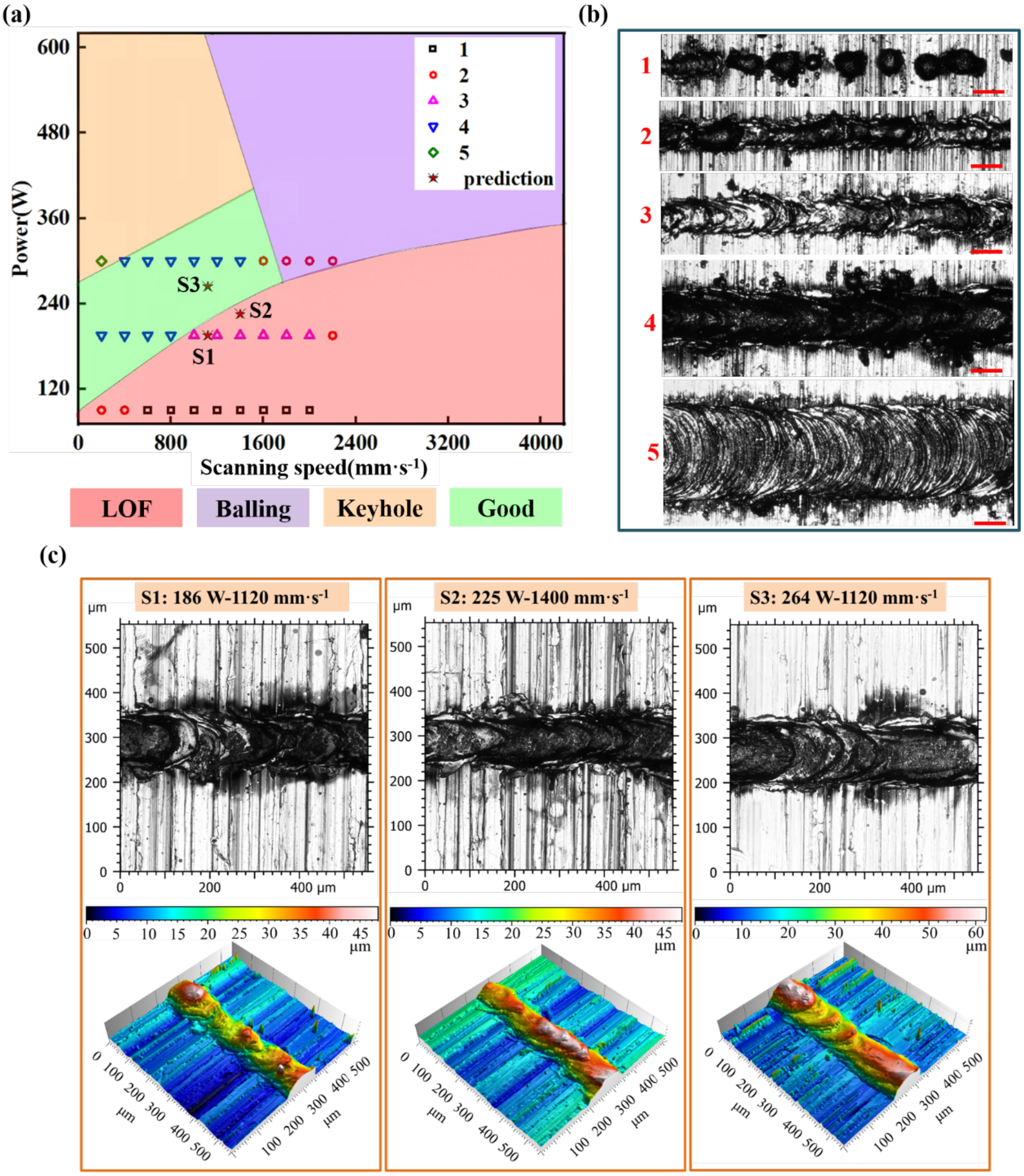

Fig. 14 (a) Printability map based on the surface topography and MP morphology, (b) typical experimental morphology and (c) experimentally surface morphology of S1, S2 and S3 in (a). Experimentally surface morphology throughout the processing parameters can be divided into 5 categories and indicated by different markers. The surface topography corresponding to numbers 1-5 is discontinuous, continuous with balling, wheat-ear shaped, raised arc-shaped fish-scale and flat arc-shaped fish-scale, respectively (Adapted from Ref. [17]). The scale bar in (b) is 100 μm.

3.2.3 Printability prediction by Machine learning

To reduce the computational time and costs while be able to give a more accurate classification result for the small sample data, different machine learning methods (DT and SVM) are adopted in this work to predict the printability of any given printing recipe and guide the printing process to fabricate components with better quality, in which the models are trained with P-V combination as input and physical-variable-based classification result as output. For a given printing recipe, the mechanistic variables are calculated by the multiphysics model, and the corresponding type is determined by the classification criteria. Thus, a connection between the input parameters and the track quality is established. The DT is constructed based on the ID3 algorithm with the entropy criterion. The maximum depth is set as three. Linear kernel function is used in the SVM algorithm. The confusion matrixes are used to demonstrate the prediction accuracy, with the column representing the true classification and the row representing the predicted classification, as shown in Fig. 15. The accuracy, precision and F1 are shown in table s4. Since it is a multiclass classification problem solved via cross-validation method, all these metrics are averages. The average prediction accuracy of DT is 0.79 with a standard deviation of 0.15. While for SVM, the average prediction accuracy and standard deviation are 0.84 and 0.2, respectively. The standard deviation is a measure of the dispersion of a dataset. A smaller standard deviation is generally preferable, which implies a more stable data group. In this context, both DT and SVM achieve relatively high prediction accuracies, but DT possesses a more robust result. As the simulation is very time-consuming, we have determined such a comprehensive model to predict the printability based on these data at present. The accuracy can be further improved by putting on more simulation work in the future. The high prediction accuracies via 10-fold cross-validation method validate the classification criterion and the comprehensive framework to assess the printability.

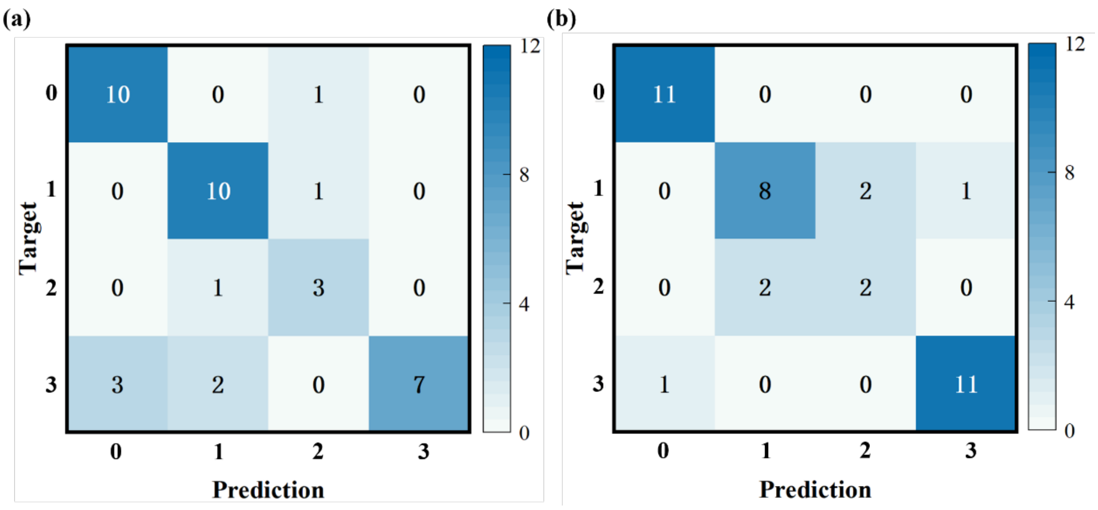

(a)

Target \ Prediction	0	1	2	3
0	10	0	1	0
1	0	10	1	0
2	0	1	3	0
3	3	2	0	7

(b)

Target \ Prediction	0	1	2	3
0	11	0	0	0
1	0	8	2	1
2	0	2	2	0
3	1	0	0	11

Fig. 15 Confusion matrices to evaluate prediction ability of (a) DT and (b) SVM. ‘Target’ represents the target output of the machine learning, which is one of the actually phenomena (balling, good, keyhole and LOF). ‘Prediction’ represents the predicted output of the machine learning. ‘0’, ‘1’, ‘2’, and ‘3’ represent balling, good, keyhole and LOF, respectively. The prediction accuracies for DT and SVM are 0.79 and 0.84, respectively.

Conclusion

In this work, a comprehensive framework including multiphysics model, physics-informed machine learning, and experimental data is proposed to predict the printability. The characteristics for different phenomena are analyzed by the mechanistic model. Then, process map is determined based on the classification criterion established by three mechanistic variables. In order to guide the AM process more conveniently in practical applications, for the first time, the relationship between the solidified-track surface morphology and the interior quality is established. The printability is predicted by mathematical machine learning classification models. This high-fidelity comprehensive framework to assess the printability could potentially guide the alloy design and printing parameters selection towards mass additive manufacturing production. The main conclusions are as follows:

1. LOF defect results from insufficient heat input, resulting shallow and small MP that can neither penetrate the substrate deeply, nor wet the substrate well, causing weak bonding and LOF voids. The MP depth is a meaningful indicator for LOF defect.

2. Keyhole occurs under high laser power and small scanning speed, resulting in longitudinally elongated MP shape. With the increase of the energy density, the longitudinal direction exhibits a larger increase rate than the transverse direction, indicating that $d/w2$ is the characteristic index of keyhole. The fluid flow in the keyhole state can be divided into two stages: 1) the counterclockwise flow when the keyhole depth increases; 2) the forward flow at the bottom and top of MP when the keyhole depth decreases.

3. Balling occurs under high scanning speed and possesses an elongated MP shape along the laser movement, in which the MP aspect ratio is a characteristic indicator to distinguish the balling from other phenomena. The most significant

feature for balling is the dynamic evolution of MP, which can be divided into two stages: expansion and pinched off.

4. The process map is determined and classified into four regions (LOF, good, balling and keyhole) after the determination of the classification procedure based on three mechanistic variables. The relationship between the surface morphology and the interior quality is established for the first time, and the optimal surface morphology corresponding to defect-free printing is identified to be raised arc-shaped fish-scale. This is of great importance for guiding the actual printing process by judge the quality from the surface instead of the cross-section to improve the printing efficiency.

5. The printability is predicted using the physics-informed machine learning algorithms via 10-fold cross-validation method to reduce the computational and time costs while be able to give a more accurate classification result. The high prediction precision of DT (0.79) and SVM (0.84) validates the classification criterion and the comprehensive framework to assess the printability.

Acknowledgements

This work is sponsored by National Natural Science Foundation of China (52004160 and 52075327), Shanghai Sailing Program (20YF1419200), Natural Science Foundation of Shanghai (20ZR1427500) and Major Science and Technology Project of Huaibei (Z2020001).

Reference

[1] Khairallah S A, Anderson A T, Rubenchik A, King W E 2016 Laser powder-bed fusion additive manufacturing: Physics of complex melt flow and formation mechanisms of pores, spatter, and denudation zones Acta Mater. 108 36-45.

[2] Zhao C, Parab N D, Li X, Fezzaa K, Tan W, Rollett A D, Sun T 2020 Critical instability at moving keyhole tip generates porosity in laser melting Science 370 1080-1086.

[3] Martin A A, Calta N P, Khairallah S A, Wang J, Depond P J, Fong A Y, Thampy V, Guss G M, Kiss A M, Stone K H, Tassone C J, Nelson Weker J, Toney M F, van Buuren T, Matthews M J 2019 Dynamics of pore formation during laser powder bed fusion additive manufacturing Nat. Commun. 10 1987.

[4] Johnson L, Mahmoudi M, Zhang B, Seede R, Huang X, Maier J T, Maier H J, Karaman I, Elwany A, Arróyave R 2019 Assessing printability maps in additive manufacturing of metal alloys Acta Mater. 176 199-210.

[5] Tomus D, Rometsch P A, Heilmaier M, Wu X 2017 Effect of minor alloying elements on crack-

formation characteristics of Hastelloy-X manufactured by selective laser melting Addit. Manuf. 16 65-72.

[6] Martin J H, Yahata B D, Hundley J M, Mayer J A, Schaedler T A, Pollock T M 2017 3D printing of high-strength aluminium alloys Nature 549 365-369.

[7] Bertoli U S, Wolfer A J, Matthews M J, Delplanque J-P R, Schoenung J M 2017 On the limitations of Volumetric Energy Density as a design parameter for Selective Laser Melting Mater. Design 113 331-340.

[8] Leung C L A, Luczyniec D, Guo E, Marussi S, Atwood R C, Meisnar M, Saunders B, Lee P D 2022 Quantification of Interdependent Dynamics during Laser Additive Manufacturing Using X-Ray Imaging Informed Multi-Physics and Multiphase Simulation Adv. Sci. 9 2203546.

[9] Huang Y, Fleming T G, Clark S J, Marussi S, Fezzaa K, Thiyagalingam J, Leung C L A, Lee P D 2022 Keyhole fluctuation and pore formation mechanisms during laser powder bed fusion additive manufacturing Nat. Commun. 13 1170.

[10] Du Y, Mukherjee T, Finch N, De A, DebRoy T 2022 High-throughput screening of surface roughness during additive manufacturing J. Manuf. Process. 81 65-77.

[11] Yu G, Gu D, Dai D, Xia M, Ma C L, Shi Q 2016 On the role of processing parameters in thermal behavior, surface morphology and accuracy during laser 3D printing of aluminum alloy J. Phys. D: Appl. Phys. 49 135501.

[12] Mahmoudi M, Tapia G, Franco B, Ma J, Arroyave R, Karaman I, Elwany A 2018 On the printability and transformation behavior of nickel-titanium shape memory alloys fabricated using laser powder-bed fusion additive manufacturing J. Manuf. Process. 35 672-680.

[13] Childs T H C, Hauser C, Badrossamay M 2004 Mapping and Modelling Single Scan Track Formation in Direct Metal Selective Laser Melting CIRP Annals - Manufacturing Technology 53 191-194.

[14] Mukherjee T, Zuback J S, De A, DebRoy T 2016 Printability of alloys for additive manufacturing Sci. Rep. 6 19717.

[15] Scime L, Beuth J 2019 Using machine learning to identify in-situ melt pool signatures indicative of flaw formation in a laser powder bed fusion additive manufacturing process Addit. Manuf. 25 151-165.

[16] Qiu C, Panwisawas C, Ward M, Basoalto H C, Brooks J W, Attallah M M 2015 On the role of melt flow into the surface structure and porosity development during selective laser melting Acta Mater. 96 72-79.

[17] Chen Y, Wang H, Wu Y, Wang H 2020 Predicting the Printability in Selective Laser Melting with a Supervised Machine Learning Method Materials 13 5063.

[18] Panwisawas C, Gong Y, Tang Y T, Reed R C, Shinjo J 2021 Additive manufacturability of superalloys: Process-induced porosity, cooling rate and metal vapour Addit. Manuf. 47 102339.

[19] Wang L, Zhang Y, Chia H Y, Yan W 2022 Mechanism of keyhole pore formation in metal additive manufacturing npj Comput. Mater. 8 22.

[20] Papazoglou E L, Karkalos N E, Markopoulos A P 2020 A comprehensive study on thermal modeling of SLM process under conduction mode using FEM Int. J. Adv. Manuf. Tech. 111 2939–2955.

[21] Yu C, Jiang J 2020 A Perspective on Using Machine Learning in 3D Bioprinting International Journal of Bioprinting 6 253.

[22] Goh G D, Sing S L, Yeong W Y 2021 A review on machine learning in 3D printing applications, potential, and challenges Artificial Intelligence Review 54 63-94.

[23] Sinclair L, Leung C L A, Marussi S, Clark S J, Chen Y, Olbinado M P, Rack A, Gardy J, Baxter G

J, Lee P D 2020 In situ radiographic and ex situ tomographic analysis of pore interactions during multilayer builds in laser powder bed fusion Addit. Manuf. 36 101512.

[24] Tang C, Le K Q, Wong C H 2020 Physics of humping formation in laser powder bed fusion Int. J. Heat Mass Transfer 149 119172.

[25] Ebrahimi A, Sattari M, Bremer S J L, Luckabauer M, Römer G R B E, Richardson I M, Kleijn C R, Hermans M J M 2022 The influence of laser characteristics on internal flow behaviour in laser melting of metallic substrates Mater. Design 214 110385.

[26] Letenneur M, Kreitcberg A, Brailovski V 2019 Optimization of Laser Powder Bed Fusion Processing Using a Combination of Melt Pool Modeling and Design of Experiment Approaches: Density Control Journal of Manufacturing and Materials Processing 3 21.

[27] Mondal B, Mukherjee T, DebRoy T 2022 Crack free metal printing using physics informed machine learning Acta Mater. 226 117612.

[28] Du Y, Mukherjee T, Mitra P, DebRoy T 2020 Machine learning based hierarchy of causative variables for tool failure in friction stir welding Acta Mater. 192 67-77.

[29] Guo L P, Wei Q L, Wang H Z, Liu H J 2022 A comprehensive model to quantify the effects of additional nano-particles on the printability in laser powder bed fusion of aluminum alloy and composite Addit. Manuf. 58 103011.

[30] Xiao Y K, Bian Z Y, Wu Y, Ji G, Li Y Q, Li M J, Lian Q, Chen Z, Addad A, Wang H W 2019 Effect of nano-TiB2 particles on the anisotropy in an AlSi10Mg alloy processed by selective laser melting J. Alloys Compd. 798 644-655.

[31] Sun T, Wang H, Gao Z, Wu Y, Wang M, Jin X, Alex Leung C L, Lee P D, Fu Y, Wang H 2022 The role of in-situ nano-TiB2 particles in improving the printability of noncastable 2024Al alloy Materials Research Letters 10 656-665.

A high-fidelity comprehensive framework for the additive manufacturing printability assessment

Liping Guo[1,2], *Hanjie Liu*[1,2], *Hongze Wang*[1,2,3,*], *Qianglong Wei*[1,2], *Jiahui Zhang*[4], *Yingyan Chen*[1,2], *Chu Lun Alex Leung*[5,6], *Qing Lian*[1,2], *Yi Wu*[1,2,3,*], *Yu Zou*[4], *Haowei Wang*[1,2,3]

1 State Key Laboratory of Metal Matrix Composites, Shanghai Jiao Tong University, Shanghai, 200240, China

2 School of Materials Science & Engineering, Shanghai Jiao Tong University, Shanghai, 200240, China

3 Institute of Alumics Materials, Shanghai Jiao Tong University (Anhui), Huaibei, 235000, China

4 Department of Materials Science and Engineering, University of Toronto, Toronto, ON M5S 3E4, Canada

5 Department of Mechanical Engineering, University College London, London, WC1E 7JE, UK

6 Research Complex at Harwell, Harwell Campus, Oxfordshire, OX11 0FA, UK

*Email: Hongze Wang, hz.wang@sjtu.edu.cn; Yi Wu, eagle51@sjtu.edu.cn

Mathematical model and numerical simulation

In this section, the main governing equations and boundary conditions for modeling are explained.

Governing equations

The temperature field and velocity field will be obtained by solving the mass, momentum and energy conservation equations, shown in equations (1-3).

$$\nabla \cdot (\vec{v}) = 0 \tag{1}$$

$$\frac{\partial \vec{v}}{\partial t_s} + \vec{v} \cdot \nabla \vec{v} = -\frac{1}{\rho} \nabla p + \mu \nabla^2 \vec{v} - F_d \vec{v} + \vec{G} \tag{2}$$

$$\rho[\frac{\partial h}{\partial t_s} + (\vec{v}\cdot\nabla)h] = \nabla\cdot(k\nabla T) \tag{3}$$

here $\vec{v}$ (m· s^{-1}) is the velocity vector. t_s (s) is the time, ρ (kg· m^{-3}) is the density, p (Pa) is the pressure and μ (m^2· s^{-1}) is the kinematic viscosity. F_d (s^{-1}) is the drag force coefficient. $\vec{G}$ (m· s^{-2}) is the body acceleration due to body force. h ($\mathrm{J}\cdot\mathrm{kg}^{-1}$) is the enthalpy, k (W· m^{-1}· K^{-1}) is the thermal conductivity and T (K) is the temperature.

The evolution of gas-liquid free surface is tracked by the volume of fluid (VOF) method:

$$\frac{\partial F}{\partial t_s} + \nabla\cdot(\vec{v}F) = 0 \tag{4}$$

where F is the volume of the fluid.

Boundary condition

The laser heat source is regarded as part of the surface heat flux boundary condition, and the main energy transfer modes in the upper free surface include convection, radiation and evaporation, which can be expressed as:

$$k\frac{\partial T}{\partial \vec{n}} = q - q_{conv} - q_{rad} - q_{evap} \tag{5}$$

$$q_{conv} = h_c\left(T - T_{ref}\right) \tag{6}$$

$$q_{rad} = \sigma\varepsilon(T^4 - T_{ref}^4) \tag{7}$$

$$q_{evap} = \varphi L_v P_{atm}\sqrt{\frac{1}{2\pi RT}}exp\left[\frac{L_v(T - T_b)}{TRT_b}\right] \tag{8}$$

here q ($\mathrm{J}\cdot\mathrm{m}^{-2}\cdot\mathrm{s}^{-1}$) is the laser heat flux absorbed by the free surface, $\vec{n}$ is the surface normal vector and h_c ($\mathrm{W}\cdot\ \mathrm{m}^{-2}\cdot\mathrm{K}^{-1}$) is the heat transfer coefficient. σ ($\mathrm{W}\cdot\ \mathrm{m}^{-2}\cdot\mathrm{K}^{-4}$) is the Stefan-Boltzmann constant and ε is the radiation emissivity. For other surfaces, only convection and radiation are considered.

$$k\frac{\partial T}{\partial \vec{n}} = -q_{conv} - q_{rad} \tag{9}$$

The pressure boundary condition on the upper surface can be written as:

$$-p + 2\mu_d \frac{\partial \vec{v}_n}{\partial \vec{n}} = -P_r + \frac{\gamma}{R_k} \tag{10}$$

here $\vec{v}_n$ $(\mathrm{m} \cdot s^{-1})$ is the normal velocity vector, μ_d $(\mathrm{Pa} \cdot \mathrm{s})$ is the dynamic viscosity. P_r (Pa) is recoil pressure. γ $(\mathrm{N} \cdot \mathrm{m}^{-1})$ is the surface tension and R_k (m) is the radius of curvature. The thermo-physical properties for TiB_2-AlSi10Mg can be found in ref. [1]. The thermal and mechanical parameters for TiB_2-AlSi10Mg for LPBF simulation are shown in table s1.

Table s1. Thermal and mechanical parameters for TiB_2-AlSi10Mg for LPBF simulation.

Properties	Value
Coefficient of evaporation and condensation φ	0.01
Latent heat of evaporation L_v (J/Kg)	1.077E+07
Saturation pressure P_{atm} (Pa)	101300
Convective heat transfer h_c $(\mathrm{W/(m^2 \cdot K)})$	80
Room temperature T_a (K)	298
Stefan-Boltzman constant σ $(\mathrm{W/(m^2 \cdot K^4)})$	5.67E-08
Gas constant R (J/(Kg·K))	308
Radiation emissivity ε	0.36
Boiling temperature T_b(K)	2750
Liquidus temperature (K)	870
Solidus temperature (K)	830

Model validation

The mechanistic model was well validated with the single-track experiment result in our previous work [1]. And to further validate the robust of the model, the molten pool dimensions for another two cases are compared with the experimental results, shown in table s2. For both cases, the deviations between the simulated dimensions and the experimental dimensions are very small, which verifies the validity and robustness of the model.

Table s2 Comparison of the fusion zone dimensions between the numerical model and the experiment for two cases.

Cases	**Manners**	**Molten pool depth (μm)**	**Molten pool height (μm)**
300 W-600 mm·s^{-1}	Experimental	54	24
	Simulated	51	23
	Deviation (%)	-5.56	-4.17
300 W-1000 mm·s^{-1}	Experimental	42	32
	Simulated	39	29
	Deviation (%)	-7.14	-9.38

To combine the surface morphology with the inner quality determined based on the MP characteristics, the simulated surface morphology and the experimental topography under the same processing conditions are compared, see Fig. 3. The left column shows the simulated tracks and the right shows the experimental results. The profiles of the solidified track height along the bule dashed lines are extracted and displayed at the bottom of each subfigure to show the track fluctuation. It can be seen that balling appears under the combination of 195 W-2200 mm·s^{-1} and becomes more obvious as the power increases to 300 W for both the simulated and experimental results. The simulated tracks exhibit good consistency with the experimental results under different P-V combinations, further demonstrating the accuracy and validity of the multiphysics model.

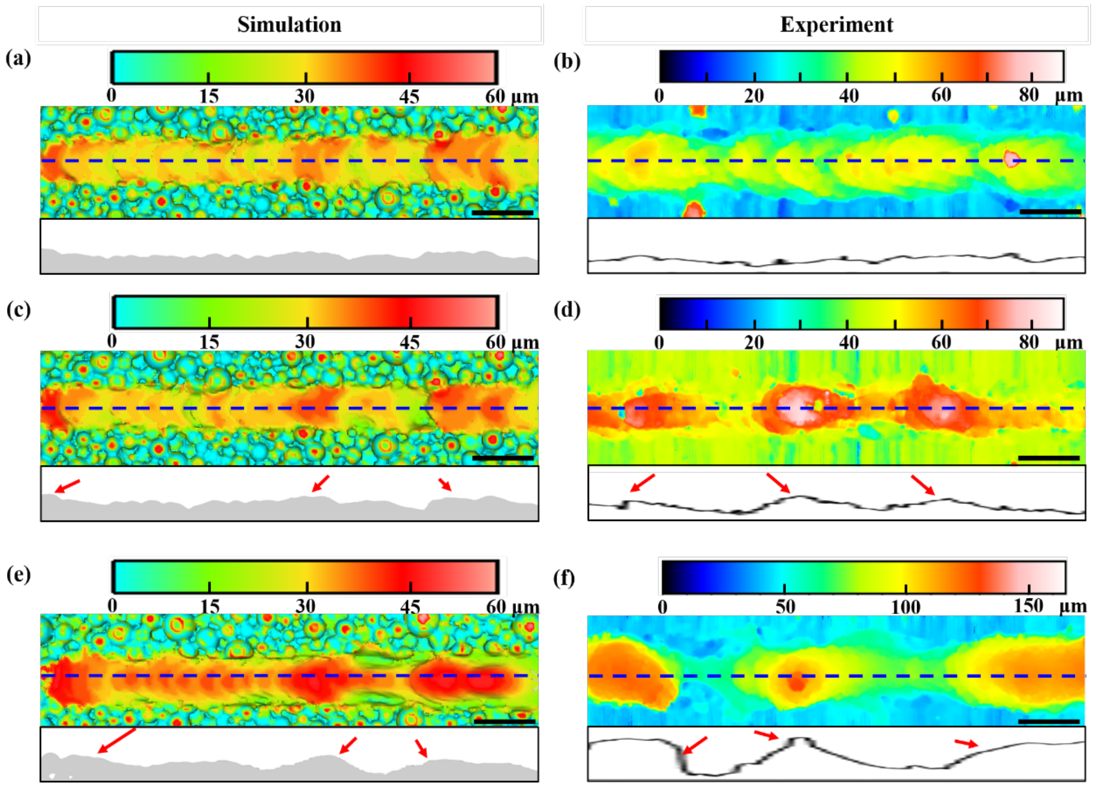

Fig. s1 Comparison of the simulated surface morphology and the experimental one under different P-V combinations for model validation (from the top view), (a) and (b) 195 W-1400 mm·s^{-1}, (c) and (d) 195 W-2200 mm·s^{-1}, (e) and (f) 300 W-2200 mm·s^{-1}. The experimental results are adapted from Ref. [2]. The insets at the bottom of each subfigure shows the profiles of the solidified track height along the bule dashed lines, in which the lower boundary of the box corresponds to the upper surface of the substrate. The red arrows indicate the humps. The scale bar is 100 µm. Color bars represent the solidified surface height.

Table s3 Dataset used in the machine learning, containing 31 data points of simulated results and 7 data points of experimental results. The letter "B" "K" "L" and "G" in the column of 'classification' refer to balling, keyhole, lack of fusion (LOF) and good, respectively. The data points 32-38 are the experimental results. '*d*/*t*' denotes the ratio of molten pool (MP) depth and layer thickness, '*d*/*w*1' is the ratio of MP depth and MP width on the upper surface of substrate, and '*l*/*w*2' is the ratio of MP length and MP width form the top view.

Data point	V (mm·s^{-1})	P (W)	*d*/*t*	*l*/*w*1	*d*/*w*2	classification
1	3000	600	1.689	2.649	0.481	B
2	3000	500	1.167	2.590	0.383	B
3	2000	500	2.103	2.634	0.573	B
4	1400	400	1.637	2.039	0.535	K
5	1000	400	1.737	1.575	0.502	K
6	600	400	2.403	1.292	0.545	K
7	3000	400	0.977	2.585	0.340	B
8	2200	300	0.777	2.230	0.317	B
9	3000	300	0.407	2.292	0.221	L
10	4000	300	0.283	2.411	0.165	L
11	1400	300	0.887	1.695	0.362	G
12	600	300	1.697	1.186	0.433	G
13	1000	300	1.060	1.377	0.352	G
14	1800	300	0.890	2.103	0.353	B
15	2000	250	0.470	1.914	0.250	L
16	1400	225	0.287	1.441	0.174	L
17	2200	195	0.170	1.666	0.134	L
18	1400	195	0.213	1.375	0.165	L
19	600	195	0.667	1.076	0.257	G
20	1000	195	0.313	1.238	0.185	L
21	1800	195	0.173	1.498	0.160	L
22	2200	90	0.000	1.259	0.000	L
23	1400	90	0.000	1.139	0.000	L
24	600	90	0.000	1.116	0.000	L
25	2000	300	0.933	2.202	0.368	B
26	1600	500	2.107	2.351	0.613	B
27	1800	400	1.503	2.330	0.495	B
28	1400	350	1.270	1.925	0.446	G
29	1800	350	1.223	2.248	0.440	B
30	1800	500	2.287	2.562	0.610	B
31	200	300	4.233	0.897	0.478	K
32	200	195	0.967		0.172	G
33	400	195	1.167		0.206	G
34	800	195	0.567		0.112	G
35	1200	195	0.367		0.092	L
36	400	300	2.200		0.325	G
37	800	300	1.433		0.257	G
38	1200	300	1.267		0.232	G

Table s4 Prediction accuracy, precision and F1 of two machine learning algorithms, accompanied with the 10-fold cross-validation method. Accuracy is the ratio of correct predictions to the total predictions. Precision (P) is the ratio of predicted positive to the true positive of all the data. Recall (R) represents the proportion of correctly predicted positive to the true positive of all the data. $F1 = \frac{2\times P\times R}{P+R}$. 'Macro' indicates that the corresponding indicator is an average value, giving all categories the same weight.

Machine learning algorithms	Macro accuracy	Standard deviation of accuracy	Macro precision	Macro F1
DT	0.79	0.15	0.78	0.77
SVM	0.84	0.20	0.78	0.78

The videos showing the dynamics of molten pool during laser powder-bed fusion of TiB_2-AlSi10Mg are as follows.

Video 1

Laser power is 90 W and scanning speed is 600 mm·s^{-1}. Belonging to LOF.

Video 2

Laser power is 195 W and scanning speed is 1400 mm·s^{-1}. Belonging to LOF.

Video 3

Laser power is 225 W and scanning speed is 1400 mm·s^{-1}. Belonging to LOF.

Video 4

Laser power is 400 W and scanning speed is 1400 mm·s^{-1}. Belonging to keyhole.

Video 5

Laser power is 400 W and scanning speed is 600 mm·s^{-1}. Belonging to keyhole.

Video 6

Laser power is 300 W and scanning speed is 4000 mm·s^{-1}. Belonging to balling.

Video 7

Laser power is 300 W and scanning speed is 3000 mm·s^{-1}. Belonging to balling.

Video 8

Laser power is 300 W and scanning speed is 2200 mm·s^{-1}. Belonging to balling.

Video 9

Laser power is 400 W and scanning speed is 3000 mm·s^{-1}. Belonging to balling.

Video 10

Laser power is 500 W and scanning speed is 3000 mm·s^{-1}. Belonging to balling.

Video 11

Laser power is 600 W and scanning speed is 3000 mm·s^{-1}. Belonging to balling.

Reference

[1] Guo L P, Wei Q L, Wang H Z, Liu H J 2022 A comprehensive model to quantify the effects of additional nano-particles on the printability in laser powder bed fusion of aluminum alloy and composite Addit. Manuf. 58 103011.

[2] Chen Y, Wang H, Wu Y, Wang H 2020 Predicting the Printability in Selective Laser Melting with a Supervised Machine Learning Method Materials 13 5063.